Geometry-driven migration efficiency of minimal cell clusters

Eléonore Vercurysse[#1], David B. Brückner[#2], Manuel Gómez-González[3], Marine Luciano[1], Yohalie Kalukula[1], Leone Rossetti[3], Xavier Trepat[3,4,5,6], Edouard Hannezo[2*] and Sylvain Gabriele[1*]

[1] Mechanobiology & Biomaterials group, Interfaces and Complex Fluids Laboratory, Research Institute for Biosciences, CIRMAP, University of Mons, Place du Parc, 20 B-7000 Mons, Belgium

[2] Institute for Science and Technology Austria. Am Campus 1, A-3400 Klosterneuburg, Austria

[3] Institute for Bioengineering of Catalonia (IBEC), The Barcelona Institute for Science and Technology (BIST), 08028 Barcelona, Spain.

[4] Centro de Investigación Biomédica en Red en Bioingeniería, Biomateriales y Nanomedicina (CIBER-BBN), 08028 Barcelona, Spain.

[5] Facultat de Medicina, Universitat de Barcelona, 08036 Barcelona, Spain.

[6] Institució Catalana de Recerca i Estudis Avançats (ICREA), Barcelona, Spain.

[#]Contributed equally to this work

*To whom correspondence should be addressed: edouard.hannezo@ist.ac.at and sylvain.gabriele@umons.ac.be

The directed migration of epithelial cell collectives through coordinated movements is key to many physiological and pathological processes and is increasingly well understood at the level of large confluent monolayers. Numerous migration processes rely on the migration of small groups of polarized epithelial clusters and their responses to external geometries. However, the interplay of cell-cell interactions and external boundaries in small cell clusters remain poorly understood. To tackle this, we used micropatterned stripes to investigate the migration of small epithelial clusters with well-defined geometries. Here we show that their migration efficiency is strongly dependent on the contact geometry, and in particular whether cell-cell contacts are parallel or perpendicular to the direction of migration. By systematically screening possible interaction mechanisms in a minimal active matter model, we show that a combination of velocity and polarity alignment with contact inhibition of locomotion captures the experimental data, which we then validated via force and intracellular stress measurements, as well as perturbations. Altogether, our results highlight the importance of geometry in defining the migration properties of cell clusters, providing a conceptual framework to extract interaction rules from how active systems interact with physical boundaries.

Collective cell migration is a fundamental process in many physiological and pathological events, such as wound healing[1], cancer metastasis[2 3 4] and morphogenesis[5 6 7]. Although the migration behavior and mechanisms of large-scale epithelial sheets has been under intense investigation in the past decades both *in vivo*[6] and *in vitro*[8 9], a number of physiologically relevant examples involve instead small clusters migrating with complex geometries and boundary conditions[10 11]. For instance, *in vivo* experiments in *Drosophila* indicated that the migration of small groups of few cells of approximately 20 μm in border cell

migration of *Drosophila* to larger groups of approximately 100 μm in the posterior lateral line primordium of zebrafish[6 12]. In addition, highly polarized and persistent locomoting tumoral clusters of up to 8 cells were observed in patients with epithelial-originating cancers or carcinomas[2 13] and in mesenchymal and epithelial cancer explants originating from various organs[3 14].

The migration of epithelial clusters requires front-rear polarization at the single-cell level through the formation of cryptic lamellipodia[15] and the establishment of a large-scale coupling between cells through axial and lateral intercellular adhesive interactions[8 16 17 18]. Different interaction rules have been proposed to describe the mechanisms underlying collective migration in large epithelial tissues, such as polarity alignment (PA), velocity alignment (VA), stress-polarity coupling (SPC) and contact inhibition of locomotion (CIL)[19 20 21 22 23 24 25]. From an active matter perspective, many of these possible interaction types give very similar predictions for the collective behavior of large monolayers[26] making it hard to test each of them rigorously. Studying the behavior of small clusters of cells and their response to well-defined geometrical boundary conditions could give key insights in the regulation of collective motion through cell-cell interactions. However, deciphering their individual role in the migration of small epithelial clusters remains challenging both theoretically and experimentally.

To tackle this, we designed a set of experiments to systematically vary the size and aspect ratio of small epithelial cell clusters by placing a fish scale containing primary epithelial tissues on flat substrates functionalized with adhesive microstripes of fibronectin of various widths (Fig. 1a). After few hours of explant culture, a large tissue of primary epithelial keratocytes grew over the micropatterns and formed fingers of cells that broke down into epithelial clusters of varying dimensions. We first concentrated on 15 μm wide microstripes, as it allows to form one-dimensional epithelial trains that lack lateral intercellular interactions

(Fig. 1b). We exploited the variability of cell train geometries to study whether the length of these minimal epithelial clusters can affect their migration speed (Fig. 1c).

As reported for individual keratocytes[27], cell trains were highly polarized, persistent and compacted (Supplementary Movies S1 and S2). Indeed, cell trains were characterized by an area proportional to the number of cells but significantly lower than the sum of the individual cell areas (Extended Data Fig. 1a). In addition, we found that keratocytes extended cryptic lamellipodia under the cell body in front of them[28] (Extended Data Fig. 1b), which have been shown to be involved in polarization and cell sheet movement[15]. We then tracked the migration of cell trains of different lengths ($2 \leq L \leq 10$ cells) to determine whether their migration speed was modulated by the number (L) of constitutive cells (Fig. 1d). Interestingly, the projected areas of these cell trains were constant over time regardless their length, demonstrating that they moved as a cohesive and single unit (Extended Data Fig. 1c). Our findings showed that the migration speed of cell trains of different lengths was similar to the speed of individual cells on 15 μm wide microstripes[27] and did not depend on the number of cells that composed the train (Fig. 1e). This suggests that intercellular axial contacts - defined as front to rear cell contacts in the direction of migration - do not influence global migration efficiency, which is in stark contrast to the much lower cell velocities of tissue-level cell migration (characterized by both axial and lateral contacts, Extended Data Figs. 1d-f). These findings also contrast with the classic view that cells far from the leading edge would behave as less migratory "follower" cells, as this would theoretically predict a decrease of global velocity with the train length L (with a 1/L trend, see Fig. 1f), instead suggesting a model where all cells are equally polarized (Fig. 1f). To confirm this, we used the mitochondrial potential membrane as a readout of the cell polarization. Indeed, it was shown that cell polarization requires increased cellular energy[29] and that the mitochondrial activity promotes cell migration by supporting membrane protrusion and modulating F-actin polymerization[30]. Stationary and unpolarized keratocytes exhibited a

rounded shape and a low MitoTracker (MT) intensity that increased immediately with their polarization (Fig. 1g, Extended Data Figs. 2a-b and Supplementary Movie S3). Interestingly, all cells within migrating cell trains of different lengths showed a large MT signal (Fig. 1h), reflecting a high level of mitochondrial activity that we found to be constant over time during the migration (Extended Data Fig. 2c). In addition, our results indicated a linear correlation between MT intensity and cell train areas (Fig. 1i), independent of the train length. Altogether, these findings indicate that all members of cell trains are metabolically active, polarized and contribute to the migration process, driving length-independent collective motion of cell trains.

We next sought to investigate the role of lateral adhesive interactions in collective migration, that were missing in one-dimensional cell trains. To this aim, we examined larger clusters of primary epithelial cells that formed on 30, 45 and 100 µm wide microstripes from an explant (Fig. 2a). The epithelial tissues grew on FN microstripes and fragmented in epithelial clusters of controlled widths (Fig. 2b) that were composed of compacted cells with cryptic lamellipodia (Extended Data Figs. 3a), as observed in the primary epithelial tissue (Extended Data Fig. 3b). Time-lapse experiments indicated that these migrating epithelial clusters of various widths were highly persistent (Supplementary Movies S4 and S5). The constituent cells of these clusters exhibited directed motion along the main axis of the microstripes (Fig. 2c), suggesting that the relative cell position within the cluster was maintained during the whole migration process, regardless the cluster width. Strikingly, widening the cell cluster to 30 µm, 45 µm and 100 µm strongly decreased the migrating velocity from 8.1±3.9 µm/min (n=59) for cell trains on 15 µm to 3.3±1.2 µm/min (n=51) on 30 µm, 2.5±0.8 µm/min (n=118) on 45 µm and 2.2±0.8 µm/min (n=64) on 100 µm (Fig. 2d), slowly converging towards the migration speed of large-scale epithelial tissues (1.4±0.4 µm/min, Extended Data Fig. 1g). This was unlikely to be due to neighbor-driven confinement as we found similar cellular densities within the different epithelial cluster sizes (Fig. 2e). Altogether, these findings suggests that lateral

cell-cell adhesive interactions have drastically different consequence – compared to axial interactions – in collective cell migration.

To shed light on the role of the cell-cell adhesions in this behavior, we induced chemical disruption of cell-cell junctions with triethylene glycol diamine tetraacetic acid (EGTA) (Extended Data Figs. 4a-b)[31]. After EGTA treatment, we observed a fragmentation of all epithelial clusters into individual cells. Interestingly, EGTA treatments performed on 30 μm wide clusters and primary tissues induced a speed up of the cells, whereas the cell migration speed remained constant after EGTA treatment on single cells and 15 μm wide clusters (Extended Data Fig. 4c). Altogether, these data argue that the establishment of an increasing number of lateral, but not axial, contacts decreases migration speed during collective migration.

The observation of length-independent but width-dependent collective motion suggests an intricate interplay of cell-cell interactions with the cell cluster geometry. From a theoretical perspective, various interaction types have been proposed in the context of collective migration[26], but it is unclear which interactions are required to capture the migration dynamics of small confined epithelial clusters. To disentangle the role of these interactions, we developed a minimal theoretical model of confined cell clusters. Based on our observations that cells in trains and clusters are polarized and exhibit few cellular re-arrangements and density variations, we modelled cells as polar particles exerting active migration forces in a direction of polarity $\boldsymbol{p}$ (defined in our system by the orientation of the lamellipodia), with each cell i connected to its neighbors j by elastic links (adhesions). This model is described by the non-dimensionalized equation $\mathrm{d}\boldsymbol{x}_i/\mathrm{d}t = \sum \boldsymbol{F}_j^{\mathrm{elastic}} + \boldsymbol{p}_i(t)$. Importantly, this model allows cell velocities $\mathrm{d}\boldsymbol{x}_i/\mathrm{d}t$ and polarities $\boldsymbol{p}_i$ that are not necessarily equal, due to cell-cell mechanical interactions. The evolution of the cell polarity can then be generally modelled as $\mathrm{d}\boldsymbol{p}_i/\mathrm{d}t = \boldsymbol{p}_i(1 - |\boldsymbol{p}_i|^2) + \boldsymbol{F}^{\mathrm{int}} + \sqrt{2D}\boldsymbol{\eta}_i(t)$, where the first term describes the spontaneous polarization of single cells, and $\boldsymbol{\eta}_i(t)$ is Gaussian white noise (see Supplementary Theory Note for details)[32].

The general interaction term $\boldsymbol{F}^{\mathrm{int}}$ subsumes many possible cell-cell interactions that could give rise to the intricate collective dynamics of confined cell clusters observed here (Fig. 2f). Two classes of interactions that have been particularly studied are neighboring cells either aligning or anti-aligning relative to each other[20 26 33]. Indeed, in our system, two-cell collision experiments can show both alignment (Extended Data Fig. 5a) and anti-alignment (Extended Data Fig. 5b) depending on the initial configuration[34 35]. Theoretically, on the one hand, alignment is motivated by the tendency of cells to "flock" in the same direction, which can be described by i) alignment of the polarity of each individual cell to match its own velocity (velocity alignment, VA)[24 26 36] and ii) direct polarity alignment (PA) between neighbors, in analogy to spins in magnetism[37 38]. On the other hand, a number of cell types have been shown to anti-align to counter-act the forces exerted by their neighbors, either due to i) stress-polarity coupling (SPC) where cells exert polarity forces opposite to stress applied on their cell-cell contacts[32 18 39] or ii) contact inhibition of locomotion (CIL), which tends to direct polarity away from cell-cell contacts[21 23 40]. We enumerate all possible couplings allowed by symmetry within our minimal model and show that they correspond to each of these categories (Supplementary Theory Note). This motivates a key question: could several distinct interaction types interplay to generate the observed nontrivial coupling to cluster geometry?

We thus proceeded to simulate clusters with varying cluster lengths and widths, under each of the possible combinations of interaction types. Generically, alignment interactions (PA or VA) lead to geometry-independent speed with all cells moving together in a specific direction, while anti-alignment interactions (SPC or CIL) induce rapidly decreasing speed with increasing length and width as clusters tend to develop a bidirectional polarity pattern (Fig 2g, Supplementary Movie S6). However, we reasoned that combining different mechanisms – to give rise to alignment in the axial direction and anti-alignment in the lateral direction – could be a promising avenue to explain our data. Interestingly, the screen of different computational

models revealed that pair-wise combinations of interactions could still not qualitatively capture our observations (Supplementary Theory Note, Supplementary Movie S7), but that the combination of VA, PA, and CIL represents the minimal interactions necessary to reproduce length-independent, but width-dependent migration (Fig. 2h). Qualitatively, this combination of interactions causes length-independent aligned cell motion in the axial direction, while the presence of boundaries along the lateral direction renders such an aligned state impossible, allowing lateral anti-alignment to develop, driven by the tendency from CIL of boundary cells to polarize outwards (Fig. 2g). Here, velocity and polarity alignment play distinct roles: while VA breaks the symmetry between axial and lateral directions, as non-zero global velocities cannot arise in the lateral direction; and PA propagates the CIL-driven laterally outwards-pointing polarity into the bulk. This causes a re-orientation of polarity at the detriment of "productive" motion which can only occur in the axial direction. In the case where VA and CIL have similar magnitudes, this interplay of geometry and interactions then gives rise to the observed trends of speed independent of length but decreasing with width (Figs. 2h,i, Supplementary Movie S8).

Our model then makes a clear and experimentally testable prediction: the outward polarization induced by CIL at the boundary and propagated by PA causes a build-up of lateral inter-cellular stress, which should increase with increasing width. To test this key prediction, we performed traction force microscopy (TFM) experiments to quantify the orientation of the traction forces generated by cell clusters of different geometries. To separate axial (along the microstripe axis) and lateral (perpendicular to the microstripe axis) components of the traction stresses (Fig. 3a), we plotted tractions in a reference frame where the horizontal and vertical axes (x, y) correspond to length and width of the cell cluster, respectively. As shown in Fig. 3b, cell trains were characterized by a dipole of forces concentrated at both extremities of the cell train and directed inward toward the center of the train, implicating a strong intercellular

coupling[8]. Interestingly, widening cell clusters to 45 and 100 μm led to the generation of more pronounced lateral traction forces. By calculating the strain energy as the dot product of the traction force with the displacement (Fig. 3c), we determined the individual contribution of axial (E_x) and lateral (E_y) components of the strain energy. In agreement with a dipole of forces, we found that cell trains on 15 μm wide microstripe exhibited a large axial component, which accounted for ~96.7% of the total strain energy (Fig. 3d) while the lateral component was negligible (~4.3%). Interestingly, the lateral component E_y increases with width, even leading to an inversion of the major strain energy component for 100 μm wide clusters, with E_y that represented ~27.1% and ~56.4% of the total strain energy for 45 and 100 μm wide clusters, respectively (Fig. 3d). As shown in Fig. 3e, widening cell clusters leads therefore to the inversion of the major strain energy component for 100 μm wide clusters. Taken together, these findings point toward a transition between axial and lateral contractile forces as a function of the cluster width, where the larger amount of traction forces in wider cell clusters is exerted normal to the direction of migration.

As traction forces must be balanced by internal forces transmitted within and between cells, we can infer the the spatio-temporal profile of the stress tensor within the monolayer using Monolayer Stress Microscopy (MSM), and thus calculate axial (σ_{xx}) and lateral (σ_{yy}) components of the internal stress field[41 42]. Our model indicated a very small amount of lateral stress in cell trains of 15 μm wide, which increased with the cluster widening (Fig. 4a). More quantitatively, our model – with parameters fully constrained based only on the speed variations as a function of cluster geometry (Fig. 2j) – successfully predicted a significant increase of the stress ratio σ_{yy}/σ_{xx} as a function of the cluster width (Fig. 4b), in agreement with MSM experiments conducted on 15, 45 and 100 μm wide clusters (Fig. 4c). The good agreement between our theoretical (Fig. 4b) and experimental (Fig. 4e) results highlight the role of the lateral stress component in wide epithelial cluster, as well as the cooperative role of several

modes of cell-cell interaction to shape the collective migration and stress profile of small cell clusters.

This specific combination of several mechanisms with opposite effects on cell polarity raises the question of what functional consequences this could have, especially since they lead to substantial unproductive lateral stresses and thus slower collective migration. To address this question, we used our model to predict how various combinations of cell-cell interactions affect cluster behavior in response to more complex external environments. When subjected to environments with blind-ends, where cell clusters must abruptly change their polarization, we found that the repolarization behavior is strongly affected by the choice of cell-cell interactions considered in the model (Extended Data Figs. 6a-d, Supplementary Movie S9). Indeed, while VA and PA mechanisms lead to fast migration in simple straight geometries, they result in poor repolarization abilities, while, intuitively, CIL leads to slow moving clusters which however repolarize quickly when contact geometry changes. Interestingly, the parameter region that captured the experimental observations (intermediate values of all three interaction parameters), exhibits a seemingly optimal behavior with both fast straight migration and obstacle-driven repolarization (Extended Data Fig. 6d). Importantly, time-lapse experiments and quantitative cell trackings performed on epithelial clusters reaching the end of a FN stripe are in agreement with the theoretical prediction, showing fast and global repolarization of both cell trains and clusters (Extended Data Figs. 6e-j). Together, these findings strengthen the validity of the combination of VA+PA+CIL and point to a potential functional relevance of these interactions.

In summary, in this work we have combined a controlled *in vitro* micropattern approach, force measurement assays and theoretical modelling to dissect the role of contact geometry in migration behavior of small epithelial clusters. We found that not only the size of a cluster, but also its geometry and aspect ratio, was a crucial parameter in determining its migration efficiency, polarization, and state of mechanical stress. In particular, we found that axial

contacts, established in the direction of cell migration, did not impede migration speed. In contrast, lateral contacts, perpendicular to the direction of cell migration, led to a build-up of lateral polarization, as evidenced by a reorientation of traction forces and monolayer stresses, and thus decreased the migration efficiency of larger cell clusters in proportion to their width. Interestingly, this displays a similar phenomenology, but at the very different length scale of multicellular systems, to how lateral confinement regulates the migration speed of individual cells[27]. Our findings are in line with the established importance of intercellular junctions to direct collective cell migration[18 43], but reveal for the first time their different functional consequences on small cluster migration depending on their geometry relative to the direction of motion.

From a theoretical perspective, we show that while different types of cell-cell interactions give rise to similar large-scale behavior [26], introducing anisotropic boundary conditions in small clusters allows us to distinguish them and infer the functional role of each interaction in cluster migration. Indeed, in the presence of boundary conditions, different interaction mechanisms cooperate in complex ways: contact-inhibition of locomotion (CIL) induces lateral polarization to slow down clusters, polarity alignment (PA) propagates the boundary information from CIL into the bulk; and velocity alignment (VA) breaks symmetry by inducing net polarization in the free axial direction. Thus, these interactions couple the bulk state of stress and polarization in cell clusters to specific boundary conditions. Other cell types such as MDCK have been shown to display flocking behavior experimentally when placed on a ring (periodic boundary conditions)[18], while we find that they did not attain a global direction of polarization on open boundary conditions (Supplementary Movie S10), consistent with previous findings on large-scale monolayer expansion[8 44]. Interestingly, we found that our model (VA+PA+CIL) captures both of these behaviors (Supplementary Movie S11), showing more generically how the nature of boundary conditions shape cell cluster behaviors. In the

future, it will be interesting to understand at molecular and biophysical level the basis for these interactions, whether they are transduced by similar or complementary pathways at the cell-cell contacts, as well as their conservation in other cellular types. This approach could further help advance our understanding of small cluster migration *in vivo*, for instance in the posterior lateral line primordium of zebrafish[6 12] or in patients with epithelial-originating cancers or carcinomas [2 13].

Materials and Methods

PDMS-coated glass coverslips. Polydimethylsiloxane (PDMS) coated glass coverslips (170 µm thick) were fabricated by spin-coating, as previously described[45]. Briefly, PDMS was prepared from the commercially available Sylgard 184 silicone elastomer kit (Dow Corning, Midland, MI) by mixing the curing agent and the base (1:10 ratio) thoroughly for 2 min. The mixture was degassed, and spin-coated at 5000 rpm on clean 25 mm glass coverslips to obtain a thin PDMS layer of ~30 µm thick. The PDMS layer was then cured for 3 hours at 60°C, flushed with ethanol and exposed to UV illumination for 15 minutes. PDMS-coated glass coverslips were then stored in the dark at room temperature in a petri dish until use.

Microcontact Printing. PDMS stamps were used to create micropattern of fibronectin on PDMS-coated glass coverslips. A PDMS mixture (Sylgard 184, Dow Corning Midland, MI) was obtained by mixing the curing agent and the base (1:10 ratio) thoroughly for 2 min[46]. After degassing, the mixture was poured on microstructured silicon wafer which was previously functionalized with fluorosilane (tridecafluoro-1,1,2,2-tetrahydrooctyl-1-trichlorosilane, Gelest) vapors under vacuum to facilitate the removal of the PDMS layer (~1 cm thick). After curing overnight at 65°C, the PDMS block was peeled off and cut in stamps of approximately

1 cm^2. PDMS stamps were washed in an ultrasonic bath with detergent solution (Decon 90, 5%) for 30 min at 35°C, then with isopropanol (70%) for 15 min at 20°C and the stamps were dried under a nitrogen flow A solution was then prepared by mixing 40 µL human fibronectin (Merck) and 960 µL of demineralized water. A volume of 100 µL of this solution was deposited on top of each stamp for 1 h at room temperature in the dark. After gently removing the solution, a PDMS stamp were dried under nitrogen flow and placed carefully in the center of a PDMS-coated glass coverslip for 15 seconds. PDMS stamps were then gently removed with tweezers and a Pluronic solution at 5 mg/mL was incubated for 5 min at room temperature to passivate non-printed areas. Microprinted PDMS-coated glass coverslips were rinsed three times with sterile PBS and dried under nitrogen flow.

Cell culture. Fish epithelial keratocytes were obtained from the scales of Central American cichlid (*Hypsophrys Nicaraguensis*)[27 45]. Scales were gently taken off the fish and placed in the center of a microprinted PDMS-coated glass coverslips and covered with a drop of 150 µL of culture medium. The culture medium was composed of Leibovitz's L-15 medium (Thermo Fisher Scientific) supplemented with 10% fetal bovine serum (FBS, Capricorn), 1% penicillin/streptomycin (Westburg), 14.2 mM HEPES (Sigma Aldrich) and 30% deionized water were put on top of the scale. A glass coverslip of 22 mm in diameter was deposited on top of the scales and few drops of culture medium were added around the samples. Epithelial keratocytes were cultured in the dark at room temperature for 12 h.

Time-lapse imaging. Time-lapse microscopy experiments were carried out on a Nikon Ti-U inverted microscope (Nikon, Japan) equipped with a manual stage[27 45]. Differential Interference Contrast (DIC) images were taken every 3 min using a ×10, ×20 or ×40 objective and captured with a DS-Qi2 camera (Nikon, Japan) controlled with the NIS Elements Advanced Research

4.0 software (Nikon). Tracking of the cell clusters were performed with the Manual Tracking plugin on FIJI.

Drug treatment. EGTA (Sigma Aldrich) was added to the normal medium at a final concentration of 2 mM to partially chelate the calcium in the medium.

Mitochondrial membrane potential. The mitochondrial membrane potential was measured using 50 nM of the MitoTracker Red dye (Invitrogen) for 30 min at room temperature to allow dye equilibration across the plasma and inner mitochondrial membranes. For imaging, the medium containing the MitoTracker Red dye was replaced with fresh normal medium.

Immunofluorescence and confocal microscopy. Fish keratocytes were fixed and permeabilized with 4% paraformaldehyde and 0.2% Triton X-100 in PBS for 15 min at room temperature. The samples were then incubated with 1% BSA in PBS for 30 min at room temperature, followed by sequential incubation with primary and secondary antibodies diluted with 1% BSA in PBS for 45 min at 37°C. Images were collected in epifluorescence and confocal mode with a Nikon A1R HD25 motorized inverted microscope equipped with x20, x40, x60 Plan Apo (NA 1.45, oil immersion) and x100 Plan Apo silicone objectives and lasers that span the violet (405 and 440 nm), blue (457, 477, and 488 nm), green (514 and 543 nm), yellow-orange (568 and 594 nm), and red (633 and 647 nm) spectral regions. Epifluorescence images were recorded with a photometrics Prime 95B camera (Photometrics Tucson, AZ) using NIS Elements Advances Research 4.5 software (Nikon). Confocal images using small Z-depth increments (0.15 μm) were processed using NIS-Elements (Nikon, Advanced Research version 4.5).

Polyacrylamide hydrogels. Polyacrylamide gel substrates of 18 kPa were prepared as previously described[47 48]. Briefly, glass-bottom dishes (MatTek, 35 mm) were treated with a solution of 714 µL acetic acid (%), 714 µL of silane in 10 mL of ethanol (96%) for 20 min. After the removal of the solution, the dishes were rinsed twice with ethanol (96%) and dried under nitrogen flow. For 18 kPa gels, a solution of 0.65 mg of N-hydroxyethyl acrylamide (HEA) in 5 mL of PBS was prepared. 820 µL of this solution was mixed in a microcentrifuge tube (Eppendorf, 1.5 mL) with 100 µL bisacrylamide (2%), 80 µL acrylamide (40 %) and 3 µL red fluorescent carboxylate-modified beads (0.2 µm, red 580/605, Life Technologies). Degas under vacuum for at least 20 min and then 0.5 µL of N,N,N',N'-tetramethyl ethylenediamine (TEMED) with 5 µL of ammonium persulfate (APS) were added to initiate the polymerization. 25 µL of the solution was carefully put on each glass-bottom dishes and 18 mm glass coverslips (previously treated under corona) were placed on top of them. After 1 h polymerization under oxygen-free atmosphere, the coverslips were removed from the gels in hot water by using tweezers. PDMS stamps were then used to create micropattern of fibronectin on each gel. After washing the stamps in an ethanol solution (70%) for 15 min in an ultrasonic bath and drying under nitrogen flow, a Corona was used for 30 s to make them more hydrophilic. A solution was prepared by mixing 70 µL human plasma fibronectin (Merck), 20 µL green fibrinogen and 910 µL PBS. 100 µL of this solution was put on top of each stamp for 1 h at room temperature in the dark. After the removal of the solution, the stamps were dried under nitrogen flow and deposited carefully in the center of each gel. We pressed carefully on each corner of the stamp with tweezers to allow protein transfer. The printing process occurred overnight at 4°C in the dark. Stamps were then gently removed with PBS and gels were rinsed 3 times with PBS. Bovine serum albumin (BSA) solution (5 mg/mL) was then used for 4 hours at and 4°C to passivate areas without any protein on the gels followed by 3 rinses with PBS. Cells were then seeded on microprinted hydrogels.

Traction force microscopy. Fluorescent beads of 200 nm in diameter were homogeneously added in the polyacrylamide solution before polymerization and their position was imaged over time with an IX83 inverted microscope equipped with a 632/22 excitation filter (incorporated in the Spectra-X light engine), a glass dichromatic mirror (Olympus), and FF01-692/40-25 (Semrock) emission filter. A reference image was obtained after the removal of cells by trypsinization. The 2D displacement field was computed using a custom PIV implementation in Matlab (MathWorks). Traction forces were computed by finite-thickness Fourier-transform traction microscopy as described previously[44 49 50].

Monolayer stress microscopy. We employed the monolayer stress microscopy (MSM) method[42] to quantify the spatial distribution of intracellular stress in cell clusters. This method is based on force equilibrium between cell-substrate tractions and cell-cell stresses. Implementation of MSM starts with the recovery of local tractions exerted by the monolayer upon its substrate. We consider a monolayer of contiguous cells which forms a uniform sheet that is flat and thin, meaning that, compared with the lateral span of the monolayer, its height is negligible. In that case, stresses within the monolayer and underlying tractions exerted by the monolayer upon its substrate are taken to be planar with no out-of-plane contributions. The stresses everywhere in the monolayers are then determined by terms arising from tractions and boundary conditions. Since the monolayer always remains in mechanical equilibrium, Newton's laws demand that this force balance must be independent of material properties of the monolayer. MSM was implemented, as a custom-made software, in Python 3 using NumPy[51], SciPy[52], Matplotlib[53], scikit-image[54], pandas[55], pyFFTW[56], opencv[57] and cython[58].

1. Lauffenburger, D. A. & Horwitz, A. F. Cell Migration: A Physically Integrated Molecular Process. *Cell* 84, 359–369 (1996).
2. Hou, J.-M. *et al.* Circulating Tumor Cells as a Window on Metastasis Biology in Lung Cancer. *The American Journal of Pathology* 178, 989–996 (2011).
3. Friedl, P. *et al.* Migration of coordinated cell clusters in mesenchymal and epithelial cancer explants in vitro. *Cancer Res* 55, 4557–4560 (1995).
4. Weiger, M. C. *et al.* Real-Time Motion Analysis Reveals Cell Directionality as an Indicator of Breast Cancer Progression. *PLoS ONE* 8, e58859 (2013).
5. Friedl, P. & Gilmour, D. Collective cell migration in morphogenesis, regeneration and cancer. *Nat Rev Mol Cell Biol* 10, 445–457 (2009).
6. Weijer, C. J. Collective cell migration in development. *Journal of Cell Science* 122, 3215–3223 (2009).
7. Schumacher, L. Collective Cell Migration in Development. in *Cell Migrations: Causes and Functions* (eds. La Porta, C. A. M. & Zapperi, S.) vol. 1146 105–116 (Springer International Publishing, 2019).
8. Serra-Picamal, X. *et al.* Mechanical waves during tissue expansion. *Nature Phys* 8, 628–634 (2012).
9. Anon, E. *et al.* Cell crawling mediates collective cell migration to close undamaged epithelial gaps. *Proceedings of the National Academy of Sciences* 109, 10891–10896 (2012).
10. Gopinathan, A. & Gov, N. S. Cell cluster migration: Connecting experiments with physical models. *Seminars in Cell & Developmental Biology* 93, 77–86 (2019).
11. Dai, W. *et al.* Tissue topography steers migrating *Drosophila* border cells. *Science* 370, 987–990 (2020).

12. Bianco, A. *et al.* Two distinct modes of guidance signalling during collective migration of border cells. *Nature* 448, 362–365 (2007).
13. Carlsson, A. *et al.* Circulating Tumor Microemboli Diagnostics for Patients with Non–Small-Cell Lung Cancer. *Journal of Thoracic Oncology* 9, 1111–1119 (2014).
14. Cheung, K. J. & Ewald, A. J. A collective route to metastasis: Seeding by tumor cell clusters. *Science* 352, 167–169 (2016).
15. Farooqui, R. & Fenteany, G. Multiple rows of cells behind an epithelial wound edge extend cryptic lamellipodia to collectively drive cell-sheet movement. *J Cell Sci* 118, 51–63 (2005).
16. Sunyer, R. *et al.* Collective cell durotaxis emerges from long-range intercellular force transmission. *Science* 353, 1157–1161 (2016).
17. Hayer, A. *et al.* Engulfed cadherin fingers are polarized junctional structures between collectively migrating endothelial cells. *Nat Cell Biol* 18, 1311–1323 (2016).
18. Jain, S. *et al.* The role of single-cell mechanical behaviour and polarity in driving collective cell migration. *Nat. Phys.* 16, 802–809 (2020).
19. Alert, R. & Trepat, X. Living cells on the move. *Physics Today* 74, 30–36 (2021).
20. Brückner, D. B. *et al.* Learning the dynamics of cell–cell interactions in confined cell migration. *Proc. Natl. Acad. Sci. U.S.A.* 118, e2016602118 (2021).
21. Zisis, T. *et al.* Disentangling cadherin-mediated cell-cell interactions in collective cancer cell migration. *Biophysical Journal* 121, 44–60 (2022).
22. Copenhagen, K. *et al.* Frustration-induced phases in migrating cell clusters. *Sci. Adv.* 4, eaar8483 (2018).
23. Singh, J., Pagulayan, A., Camley, B. A. & Nain, A. S. Rules of contact inhibition of locomotion for cells on suspended nanofibers. *Proc. Natl. Acad. Sci. U.S.A.* 118, e2011815118 (2021).

24. Basan, M., Elgeti, J., Hannezo, E., Rappel, W.-J. & Levine, H. Alignment of cellular motility forces with tissue flow as a mechanism for efficient wound healing. *Proc. Natl. Acad. Sci. U.S.A.* 110, 2452–2459 (2013).
25. Sepúlveda, N. *et al.* Collective Cell Motion in an Epithelial Sheet Can Be Quantitatively Described by a Stochastic Interacting Particle Model. *PLoS Comput Biol* 9, e1002944 (2013).
26. Alert, R. & Trepat, X. Physical Models of Collective Cell Migration. *Annu. Rev. Condens. Matter Phys.* 11, 77–101 (2020).
27. Mohammed, D. *et al.* Substrate area confinement is a key determinant of cell velocity in collective migration. *Nat. Phys.* 15, 858–866 (2019).
28. Ozawa, M. *et al.* Adherens junction regulates cryptic lamellipodia formation for epithelial cell migration. *Journal of Cell Biology* 219, e202006196 (2020).
29. Fu, D. *et al.* Coordinated elevation of mitochondrial oxidative phosphorylation and autophagy help drive hepatocyte polarization. *Proc. Natl. Acad. Sci. U.S.A.* 110, 7288–7293 (2013).
30. Schuler, M.-H. *et al.* Miro1-mediated mitochondrial positioning shapes intracellular energy gradients required for cell migration. *MBoC* 28, 2159–2169 (2017).
31. Sotomayor, M. & Schulten, K. The Allosteric Role of the Ca2+ Switch in Adhesion and Elasticity of C-Cadherin. *Biophysical Journal* 94, 4621–4633 (2008).
32. Banerjee, S., Utuje, K. J. C. & Marchetti, M. C. Propagating Stress Waves During Epithelial Expansion. *Phys. Rev. Lett.* 114, 228101 (2015).
33. Barton, D. L., Henkes, S., Weijer, C. J. & Sknepnek, R. Active Vertex Model for cell-resolution description of epithelial tissue mechanics. *PLoS Comput Biol* 13, e1005569 (2017).

34. Dormann, D., Weijer, G., Parent, C. A., Devreotes, P. N. & Weijer, C. J. Visualizing PI3 Kinase-Mediated Cell-Cell Signaling during Dictyostelium Development. *Current Biology* 12, 1178–1188 (2002).
35. Li, D. & Wang, Y. Coordination of cell migration mediated by site-dependent cell–cell contact. *Proc. Natl. Acad. Sci. U.S.A.* 115, 10678–10683 (2018).
36. Peyret, G. *et al.* Sustained Oscillations of Epithelial Cell Sheets. *Biophysical Journal* 117, 464–478 (2019).
37. Vicsek, T., Czirók, A., Ben-Jacob, E., Cohen, I. & Shochet, O. Novel Type of Phase Transition in a System of Self-Driven Particles. *Phys. Rev. Lett.* 75, 1226–1229 (1995).
38. Debets, V. E., Janssen, L. M. C. & Storm, C. Enhanced persistence and collective migration in cooperatively aligning cell clusters. *Biophysical Journal* 120, 1483–1497 (2021).
39. Weber, G. F., Bjerke, M. A. & DeSimone, D. W. A Mechanoresponsive Cadherin-Keratin Complex Directs Polarized Protrusive Behavior and Collective Cell Migration. *Developmental Cell* 22, 104–115 (2012).
40. Abercrombie, M. Contact inhibition and malignancy. *Nature* 281, 259–262 (1979).
41. Tambe, D. T. *et al.* Collective cell guidance by cooperative intercellular forces. *Nature Mater* 10, 469–475 (2011).
42. Tambe, D. T. *et al.* Monolayer Stress Microscopy: Limitations, Artifacts, and Accuracy of Recovered Intercellular Stresses. *PLoS ONE* 8, e55172 (2013).
43. Khalilgharibi, N. *et al.* Stress relaxation in epithelial monolayers is controlled by the actomyosin cortex. *Nat. Phys.* 15, 839–847 (2019).
44. Trepat, X. *et al.* Physical forces during collective cell migration. *Nature Phys* 5, 426–430 (2009).

45. Riaz, M., Versaevel, M., Mohammed, D., Glinel, K. & Gabriele, S. Persistence of fan-shaped keratocytes is a matrix-rigidity-dependent mechanism that requires α5β1 integrin engagement. *Sci Rep* 6, 34141 (2016).
46. Versaevel, M., Grevesse, T., Riaz, M., Lantoine, J. & Gabriele, S. Micropatterning Hydroxy-PAAm Hydrogels and Sylgard 184 Silicone Elastomers with Tunable Elastic Moduli. *Micropatterning in Cell Biology Part C* 121, 33–48 (2014).
47. Grevesse, T., Versaevel, M., Circelli, G., Desprez, S. & Gabriele, S. A simple route to functionalize polyacrylamide hydrogels for the independent tuning of mechanotransduction cues. *Lab Chip* 13, 777 (2013).
48. Luciano, M. *et al.* Cell monolayers sense curvature by exploiting active mechanics and nuclear mechanoadaptation. *Nat. Phys.* 17, 1382–1390 (2021).
49. Versaevel, M., Grevesse, T. & Gabriele, S. Spatial coordination between cell and nuclear shape within micropatterned endothelial cells. *Nat Commun* 3, 671 (2012).
50. Bruyère, C. *et al.* Actomyosin contractility scales with myoblast elongation and enhances differentiation through YAP nuclear export. *Sci Rep* 9, 15565 (2019).
51. Harris, C. R. *et al.* Array programming with NumPy. *Nature* 585, 357–362 (2020).
52. Virtanen, P. *et al.* SciPy 1.0: fundamental algorithms for scientific computing in Python. *Nat Methods* 17, 261–272 (2020).
53. Hunter, J. D. Matplotlib: A 2D Graphics Environment. *Comput. Sci. Eng.* 9, 90–95 (2007).
54. van der Walt, S. *et al.* scikit-image: image processing in Python. *PeerJ* 2, e453 (2014).
55. McKinney, W. Data Structures for Statistical Computing in Python. in 56–61 (2010). doi:10.25080/Majora-92bf1922-00a.

56. Proceedings of the ACM SIGPLAN 1999 conference on Programming language design and implementation - PLDI '99. in *Proceedings of the ACM SIGPLAN 1999 conference on Programming language design and implementation - PLDI '99* (ACM Press, 1999).
57. Bradski, G. The OpenCV Library. *Dr. Dobb's Journal of Software Tools* 25, 120–125 (2000).
58. Behnel, S. *et al.* Cython: The Best of Both Worlds. *Comput. Sci. Eng.* 13, 31–39 (2011).

Acknowledgments

M.L., E.V. and S.G. acknowledges funding from FEDER Prostem Research Project no. 1510614 (Wallonia DG06), the F.R.S.-FNRS Epiforce Project no. T.0092.21 and the Interreg MAT(T)ISSE project, which is financially supported by Interreg France-Wallonie-Vlaanderen (Fonds Européen de Développement Régional, FEDER-ERDF). E.V. and Y.K. are financially supported by FRIA (F.R.S.-FNRS). This project was supported by the European Research Council under the European Union's Horizon 2020 Research and Innovation Program Grant Agreements 851288 (to E.H) and the Marie Skłodowska-Curie grant agreement 797621 (to M.G.G.). D.B.B. is a NOMIS Fellow supported by the NOMIS Foundation, and performed this work in part at Aspen Center for Physics, which is supported by National Science Foundation grant PHY-1607611. X.T. and M.G.G. acknowledge support from The Generalitat de Catalunya (AGAUR SGR-2017-01602 to and the CERCA Programme), the Spanish Ministry for Science and Innovation MICCINN/FEDER (PGC2018-099645-B-I00), the European Research Council (Adv-883739), Fundació la Marató de TV3 (201903-30-31-32), the European Commission (H2020-FETPROACT-01-2016-731957), La Caixa Foundation, and by CIBER -Consorcio Centro de Investigación Biomédica en Red- (CB15/00153), Instituto de Salud Carlos III, Ministerio de Ciencia e Innovación. IBEC is recipient of a Severo Ochoa Award of Excellence from the MINECO.

Author contributions

S.G. and E.V. conceived the project and S.G. supervised the project. E.V. developed minimal epithelial models and performed cell experiments, tracking and imaging. D.B.B. and E.H. developed the theoretical model, D.B.B. implemented and performed simulations. L.R., Y.K. and M.L. contributed to experiments. E.V., D.B.B., M.G.G., X.T., E.H. and S.G. analyzed data.

The article was written by E.V., D.B.B., E.H. and S.G., read and corrected by all authors, who all contributed to the interpretation of the results.

Competing interests

The authors declare no competing interests.

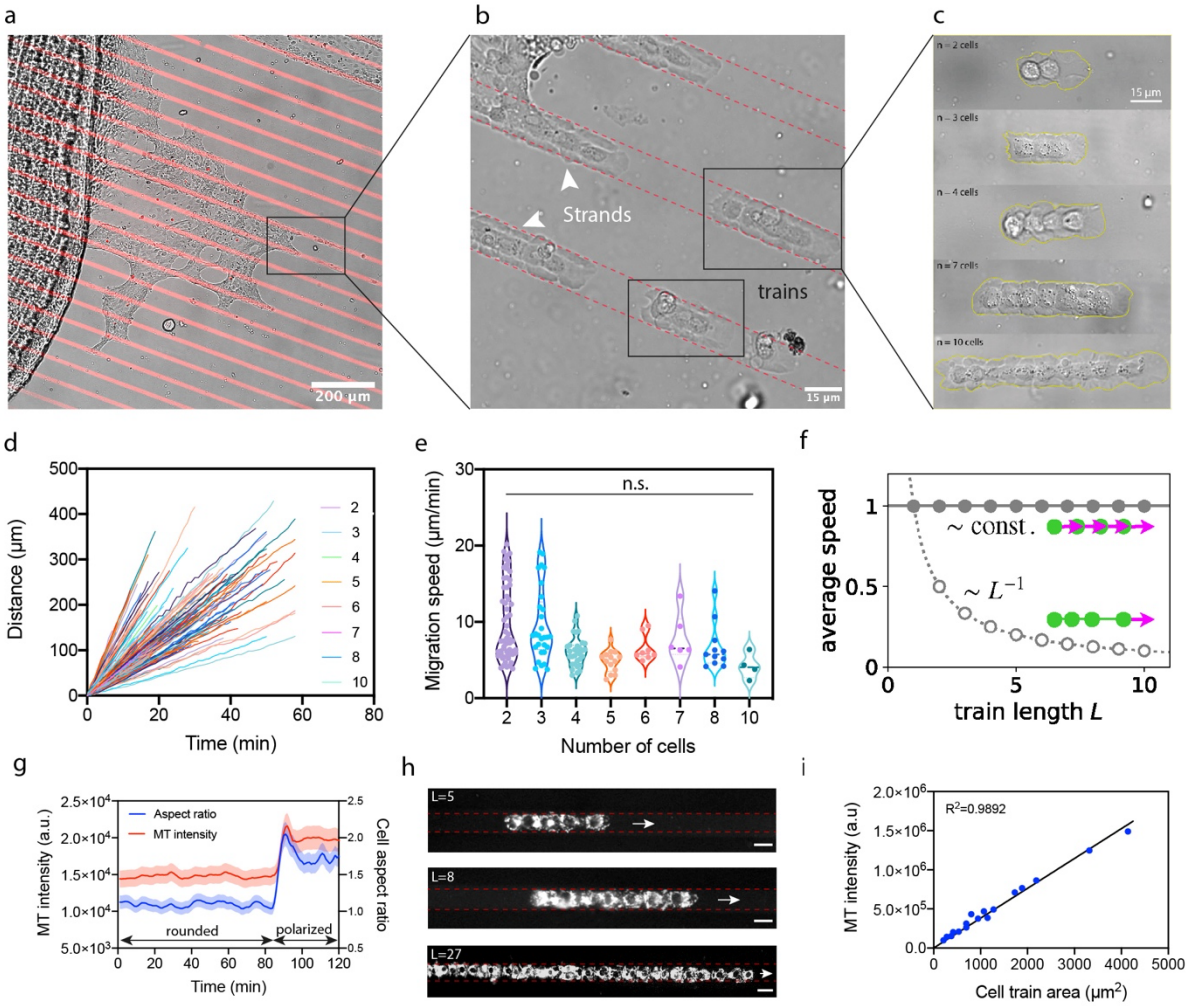

Figure 1 – The migration velocity of cell trains is not affected by their length. (a) A fish scale is deposited on a PDMS substrate covered with fibronectin (FN) microstripes of 15 µm wide (in red). **(b)** The growth of the primary epithelial tissue onto the FN microstripes leads to the formation of "strands" that break in **(c)** random-sized one-dimensional epithelial clusters called cell trains. **(d)** Temporal evolution of the migrating distance for cell trains of different sizes ($2 \leq L \leq 10$). **(e)** Migration speed of cell trains composed of different numbers of cells (from L=2 to 10, with n=285). **(f)** Prediction of the speed as function of the train length using a model of elastically coupled active particles with either all cells polarized (solid grey dots), or with the leader cell polarized only (open dots). **(g)** Temporal evolution of MitoTracker (MT) intensity (in red) and cell aspect ratio (in blue) for individual keratocytes (n=3) which

underwent a transition of polarization at t=88 min and started to migrate. **(h)** Live mitochondria staining with MT in cell trains of different lengths (L=5, 8 and 27 cells). Scale bars in are 15 µm. **(i)** The total MT intensity in cell trains is linearly proportional their area, regardless their length.

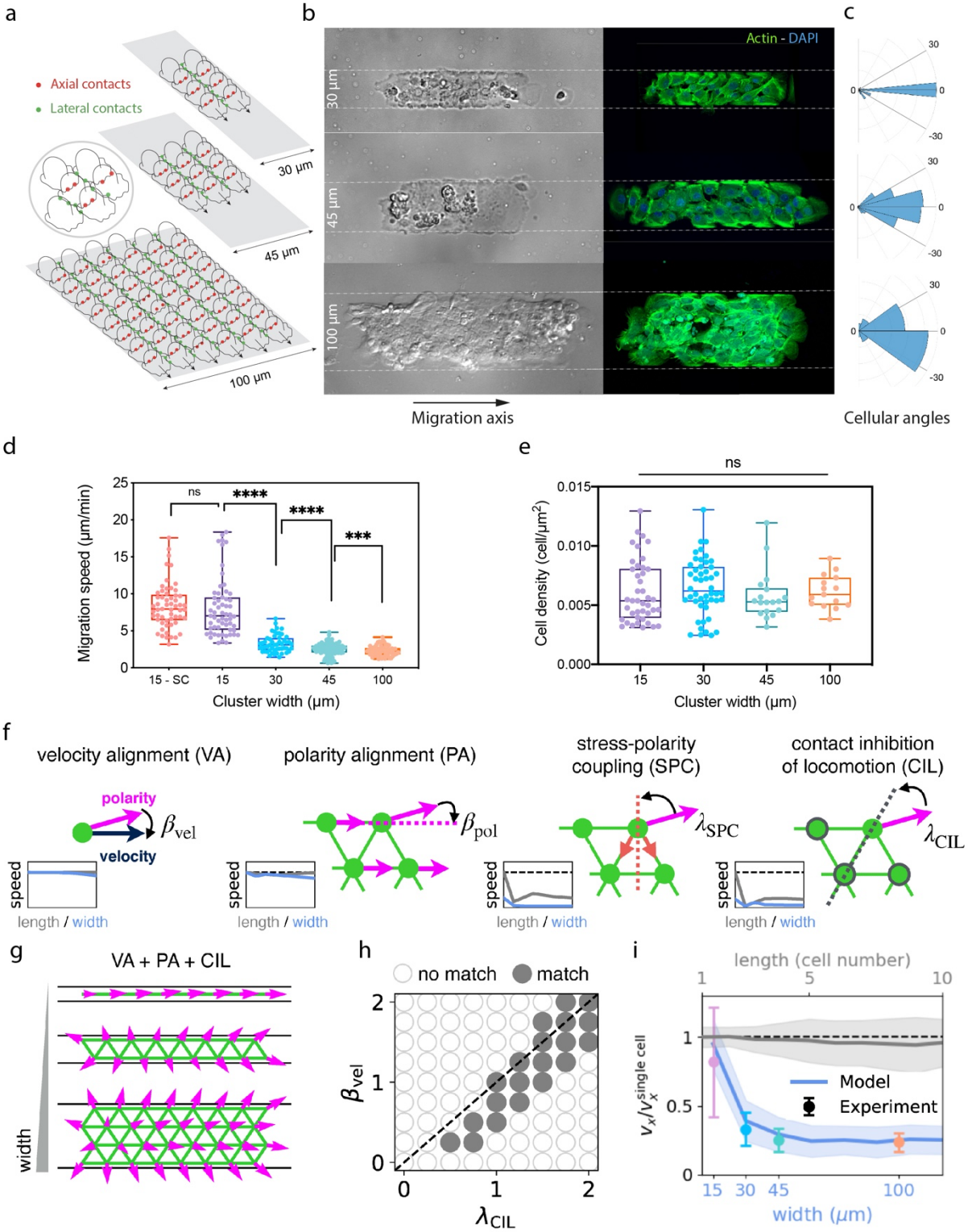

Figure 2 – The migration velocity decreases with the epithelial cluster widening. (a) Standardized cell clusters of varying widths were formed on FN microstripes of 30, 45 and 100 µm wide to impose a gradual increase of the number of cell-cell interactions. **(b)** Typical micrographs in DIC and epifluorescence mode (actin in green and DAPI in blue) of epithelial

clusters formed on FN microstripes of 30, 45 and 100 μm. **(c)** Distribution of the migration angle of each individual cell within an epithelial cluster migrating during 60 min on a 30 μm (top), 45 μm (middle) and 100 μm (bottom) wide microstripe. The axis of the microstripe (horizontal axis) corresponds to 0°. **(d)** Distribution of the migration speed for single epithelial cells on 15 μm wide microstripes (SC, in pink) and epithelial clusters on 15 μm (in purple), 30 μm (in blue), 45 μm (in green) and 100 μm (in orange). **(e)** Cell density of epithelial clusters of different widths. **(f)** Schematic illustration of each of the four considered cell-cell interaction mechanisms, from left to right: velocity alignment (VA), polarity alignment (PA), stress-polarity coupling (SPC), and contact inhibition of locomotion (CIL), quantified by amplitudes β_{vel}, β_{pol}, λ_{SPC}, λ_{CIL}, respectively (Supplementary Theory Note). Green dots and lines represent cells and elastic links between cells, respectively, and blue, magenta and red arrows denote cell velocity, polarity, and inter-cellular stress, respectively. Insets: predicted dependence of cluster speed as a function of length (grey) and width (red) for each of the mechanisms. Dashed line indicates the speed of a single cell. **(g)** Predicted polarity fields as a function of cluster width for the combination of VA, PA and CIL. **(h)** Phase diagram indicating where the VA+PA+CIL model captures the qualitative trends of speeds independent of length and decreasing with width (solid grey dots), as a function of the VA and CIL strength, for fixed β_{pol} = 1.5. Similar trends are observed for other β_{pol} (Supplementary Theory Note). **(i)** Predicted speed dependence as a function of width (red) and length (grey) for best fit parameters β_{vel} = 0.15, β_{pol} = 1.5, λ_{CIL} = 0.5, compared to experiment (blue squares). Speeds in both model and experiment are normalized by the single cell speed. Error bars denote standard deviations.

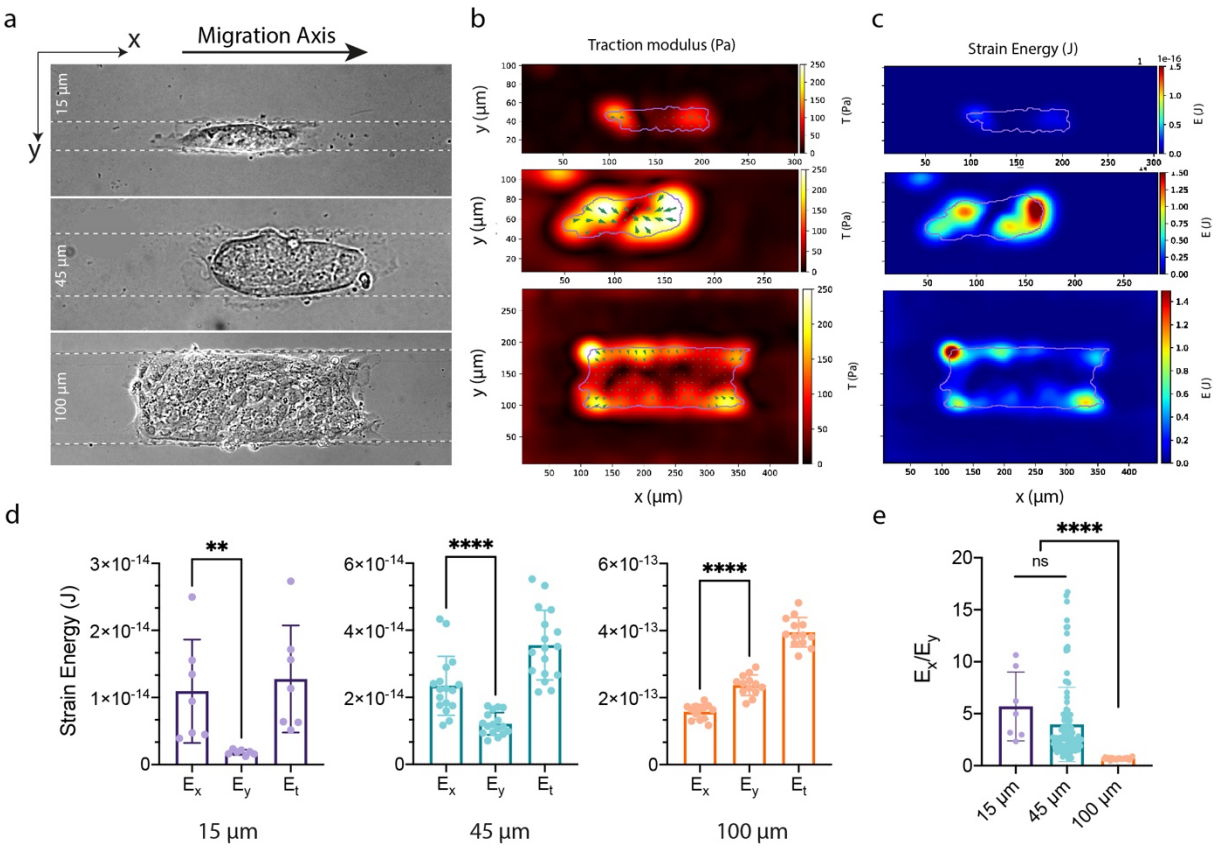

Figure 3 – Widening epithelial clusters leads to the emergence of lateral contractile forces and lateral intracellular stresses. (a) Typical DIC images of epithelial clusters on 15 µm, 45 µm and 100 µm wide microstripes. **(b)** Heat map of the spatial distribution of the traction modulus and **(c)** the strain energy field exerted on the substrate during the migration of epithelial clusters of 15 µm, 45 µm and 100 µm wide. Distribution of **(d)** axial (E_x) and lateral (E_y) components of the total strain energy (E_t) and **(e)** E_x/E_y ratio for epithelial clusters of 15 µm wide (in purple), 45 µm (in green) and 100 µm (in orange) wide. **$p < 0.01$, ****$p < 0.0001$ and n.s. not significant. Error bars denote standard deviations.

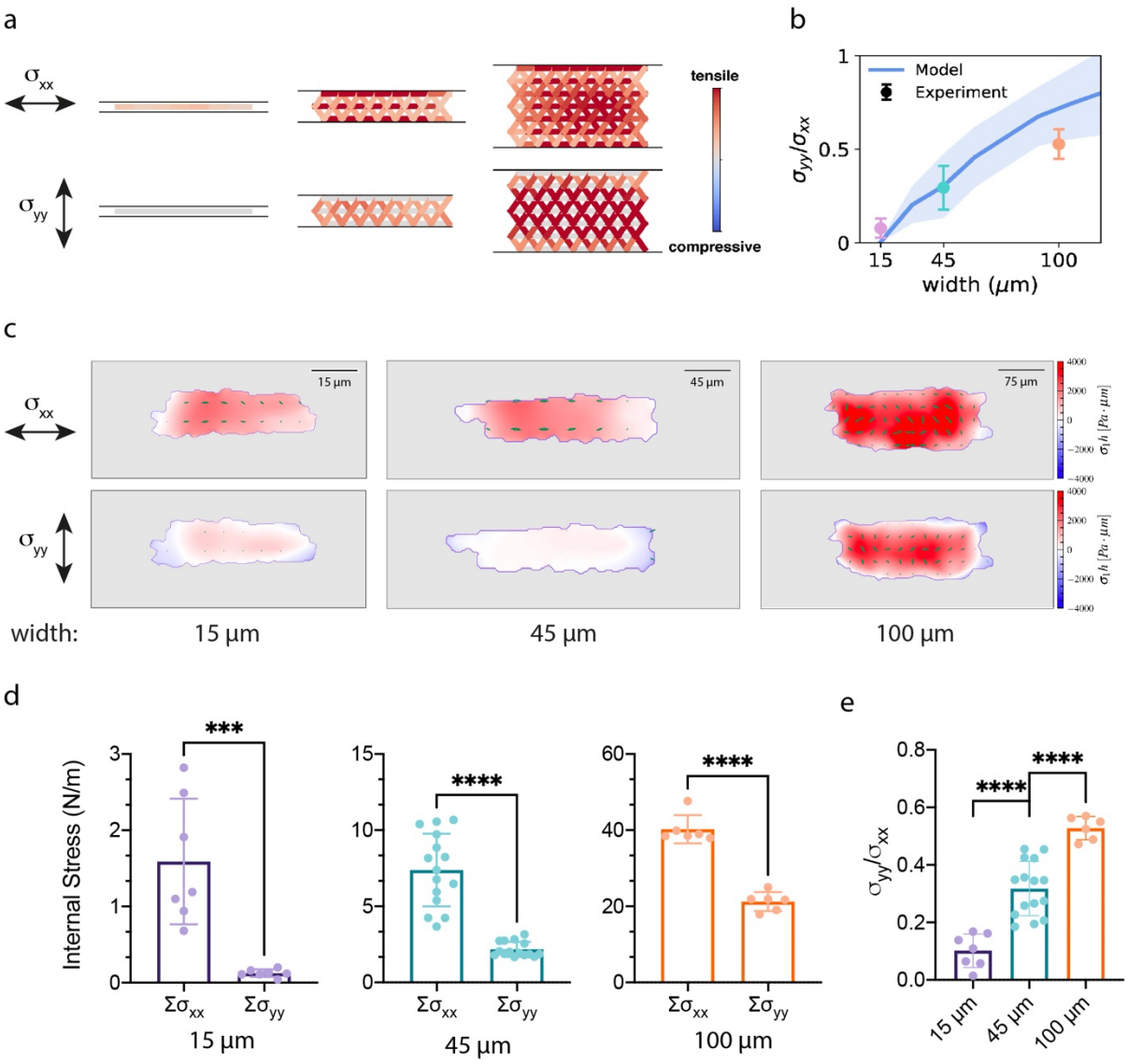

Figure 4 – The lateral internal stress increases in wider epithelial clusters. (a) Theoretical predictions of axial (σ_{xx}; top) and lateral (σ_{yy}; bottom) components of the internal stress field for varying cluster widths (1, 3 and 7 cells, corresponding to 15, 45 and 100 μm) using the VA+PA+CIL model. **(b)**. Ratio of the lateral to axial stress σ_{yy}/σ_{xx} as a function of cluster width as predicted by the model with best parameters identified based on cell speed (see Fig. 2j). **(c)** Typical maps of the spatial distribution of axial (σ_{xx}) and lateral (σ_{yy}) internal stress components for cell trains of 15 μm wide (in light purple) and epithelial clusters of 45 (in light green) and 100 μm (in light orange) wide. **(d)** Quantification of σ_{xx} and σ_{yy} and **(e)** σ_{yy}/σ_{xx} ratio. ***$p < 0.001$, ****$p < 0.0001$ and n.s. not significant. Error bars denote standard deviations.

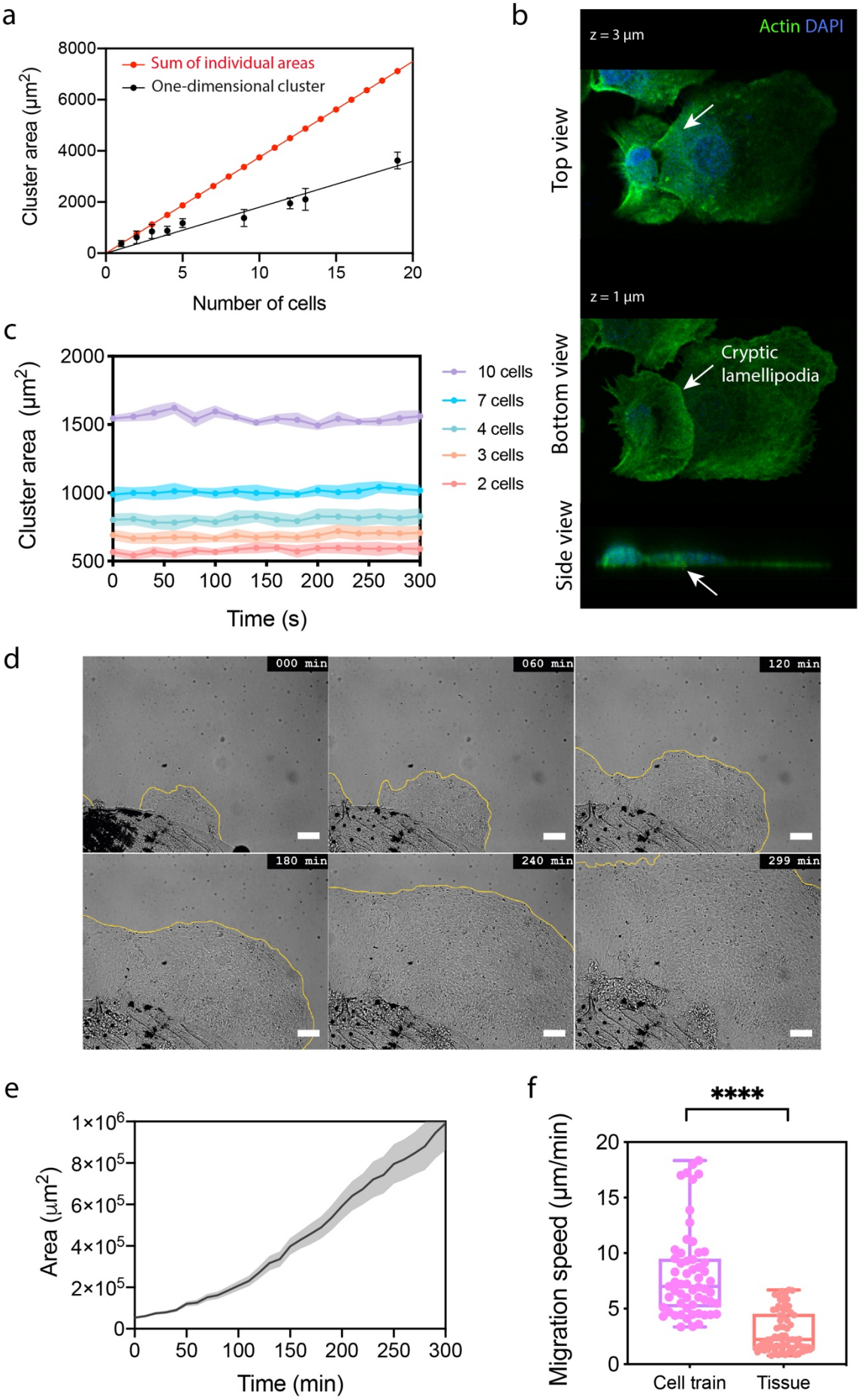
a
Sum of individual areas
One-dimensional cluster
Cluster area (μm²)
Number of cells
b
z = 3 μm
Actin DAPI
Top view
z = 1 μm
Bottom view
Cryptic lamellipodia
Side view
c
Cluster area (μm²)
Time (s)
10 cells
7 cells
4 cells
3 cells
2 cells
d
000 min
060 min
120 min
180 min
240 min
299 min
e
Area (μm²)
Time (min)
f
****
Migration speed (μm/min)
Cell train
Tissue

Extended Data Figure 1 – One-dimensional epithelial clusters are compacted and faster than tissues. (a) The cluster area is linearly correlated with the number of cells (black points) and smaller than the sum of individual cell areas (red points), suggesting that cells in one-dimensional epithelial clusters are significantly compacted. **(b)** Confocal images (top, bottom, and side views) of a cryptic lamellipodia in a cell doublet. **(c)** The cluster area is constant over time, regardless the number of cells, demonstrating that one-dimensional epithelial clusters move as a single unit. **(d)** Typical time-lapse sequence in DIC mode of a bidimensional epithelial tissue growing out of a scale during 299 min. The growing front is depicted with a yellow line. The scale bar is 100 µm. **(e)** Evolution of the tissue area over time (n=3, mean ± S.D.). **(f)** Migration speed for one-dimensional epithelial clusters ("cell train" in pink, n=62) and epithelial tissues ("tissue" in red, n=74) with ****$p < 0.0001$.

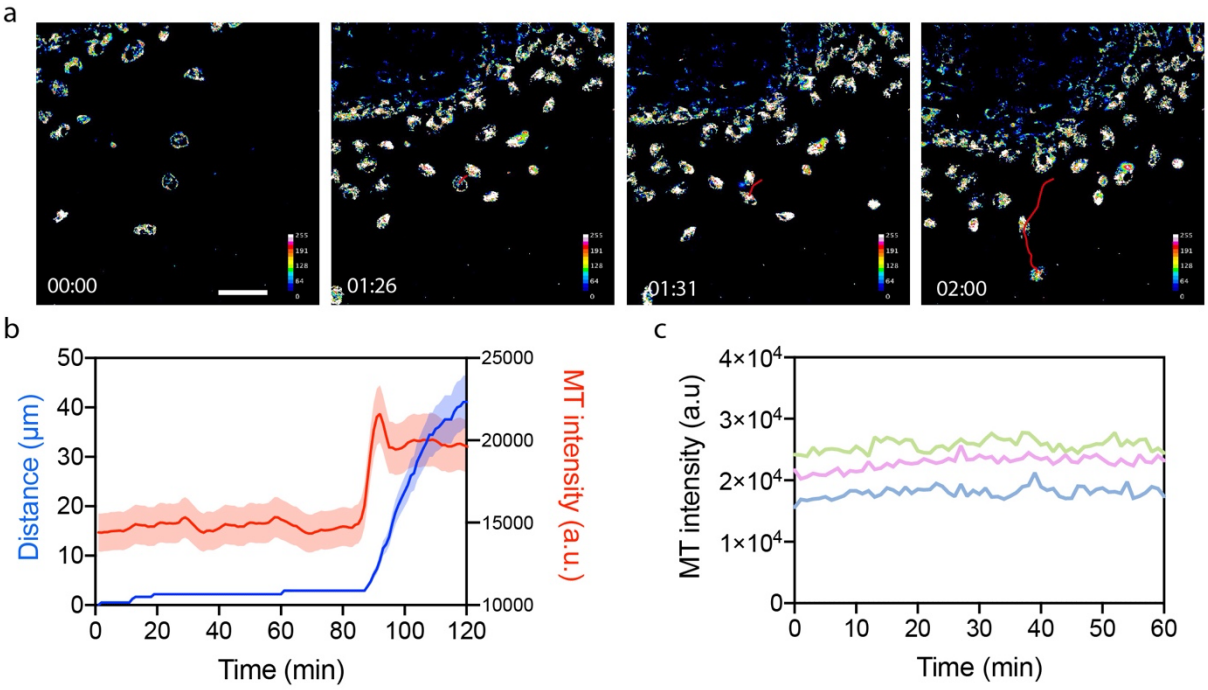

Extended Data Figure 2 – The mitochondrial membrane potential increases as the cell polarizes and remains constant during migration. (a) Typical time-lapse sequence in epifluorescence mode of single epithelial cells stained with red MitoTracker (MT). Cells were digitized in 256 bits and the MitoTracker intensity was color-coded (from high to low: white, purple, red, orange, yellow, green, light blue and dark blue). The redline shows the displacement of a cell that started to polarize and migrate at 86 min. The scale bar is 30 µm. **(b)** Evolution of the distance (in blue) and the MT intensity (in red) over time (n=3, mean ± S.D.) **(c)** Evolution of the MT intensity of three individual polarized cells that migrate during 60 min.

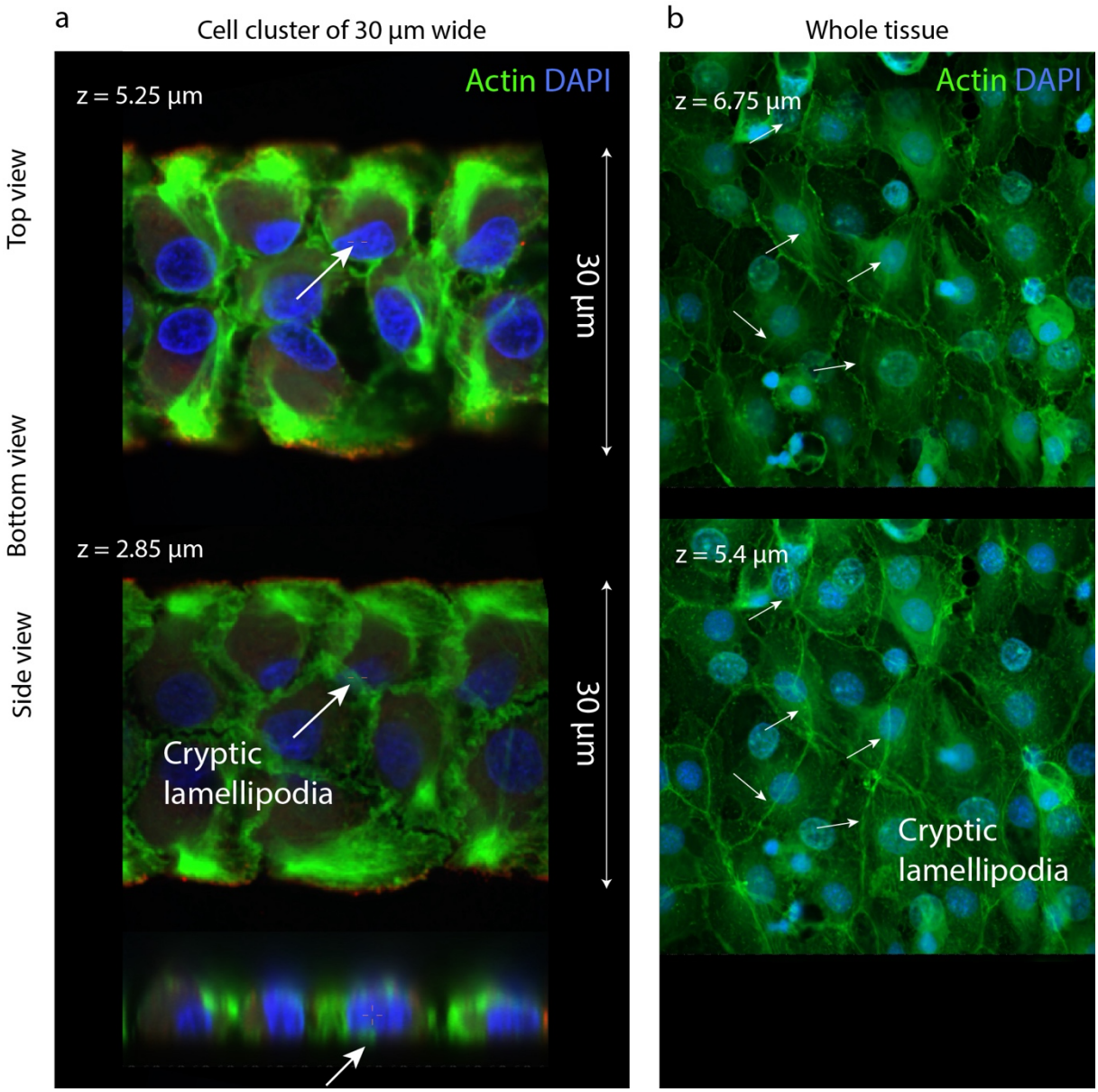

Extended Data Figure 3 – Cell clusters and epithelial tissues are composed of cryptic lamellipodia that invade underneath the adjoining cell. Confocal images (top, bottom, and side views) of cryptic lamellipodia in **(a)** an epithelial cluster of 30 µm wide and **(b)** a bidimensional epithelial tissue. Actin is labeled in green with Phalloidin and DNA in blue with DAPI. The white arrows show the position of typical cryptical lamellipodia.

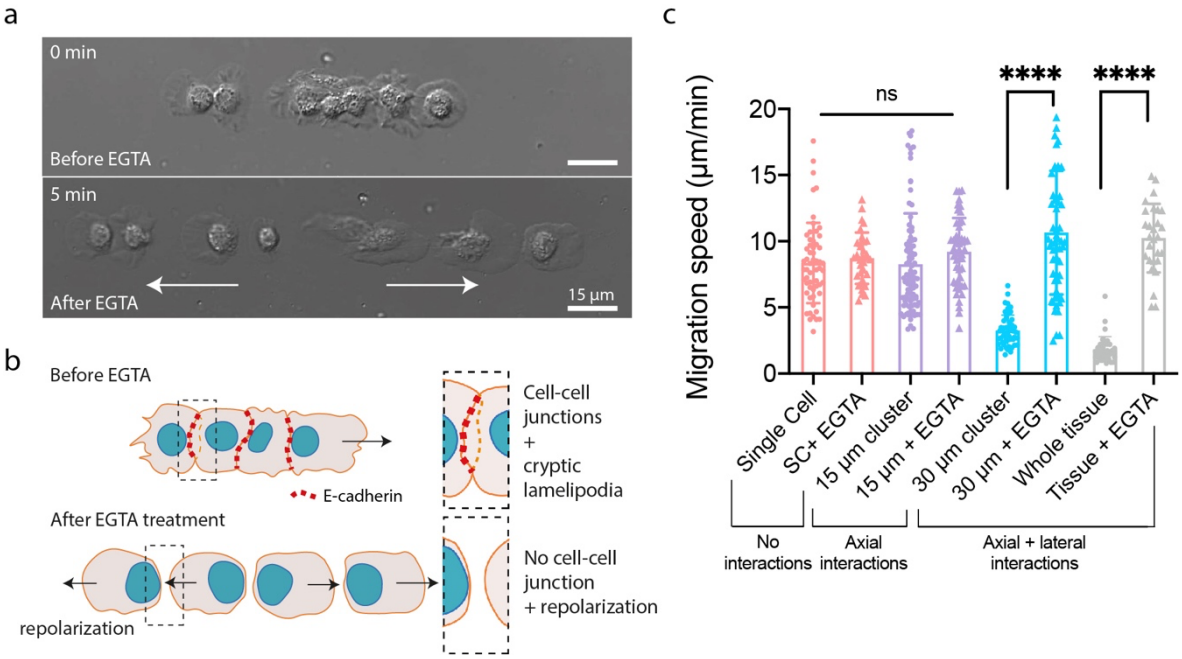

Extended Data Figure 4 – Disruption of cell-cell adhesions with EGTA treatments leads to the increase of the migration speed and repolarization events. (a) Typical microscopy images in DIC mode of a one-dimensional epithelial cluster migrating on a 15 µm wide micropatterns before (t=0 min) and after (t=5 min) EGTA treatments. White arrows show the cell repolarization. Scale bars are 15 µm. **(b)** Schematic representation of the EGTA effect that disrupts adherens cell-cell adhesions due to a weakening of the rigid extracellular domain of E-cadherin and leads to repolarization events. **(c)** Migration speed of single cells on 15 µm wide microstripes (control: n=57, EGTA: n=32, in red), cell trains on 15 µm wide microstripes (control: n=88, EGTA: n= 49, in purple), epithelial clusters on 30 µm wide microstripes (control: n=51, EGTA: n=57, in blue) and whole epithelial tissues (control: n=37, EGTA: n=28, in grey). Control data are circles and EGTA-treated data are lozenges, ns is non-significant and ****$p < 0.0001$.

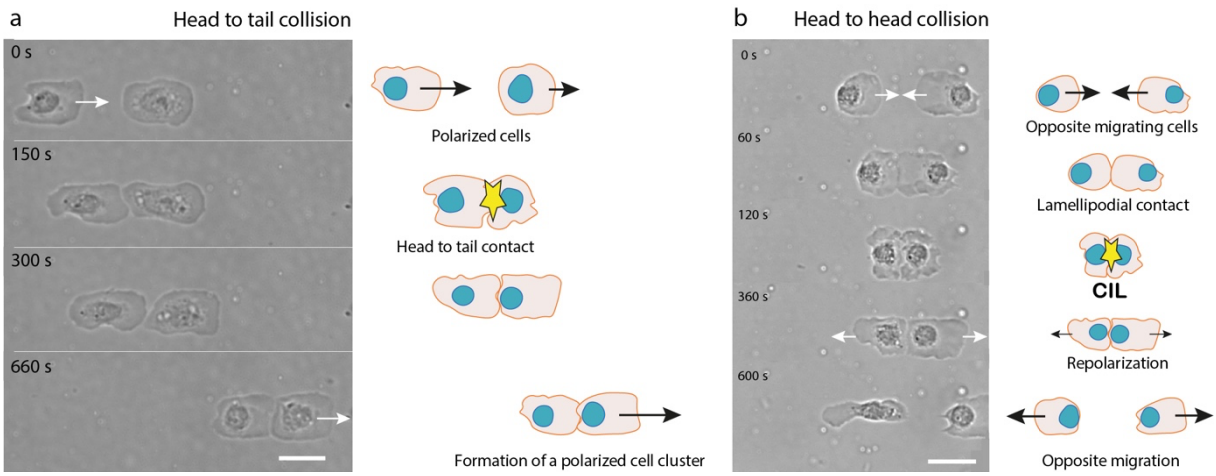

Extended Data Figure 5 – The collision configuration between two epithelial cells induced an attractive or repulsive response. (a) Head-to-tail collisions promoted to the formation of a contact between a cell lamellipodia and the tail of a neighboring cell, leading to the formation of a polarized cell doublet, suggesting that head-to-tail collisions can promote the formation of larger cell clusters. **(b)** The contact inhibition of locomotion (CIL) was observed during head-to-head collisions between individual epithelial cells moving on 15 µm wide, showing a repulsive response of both cells that repolarized rapidly in opposite directions.

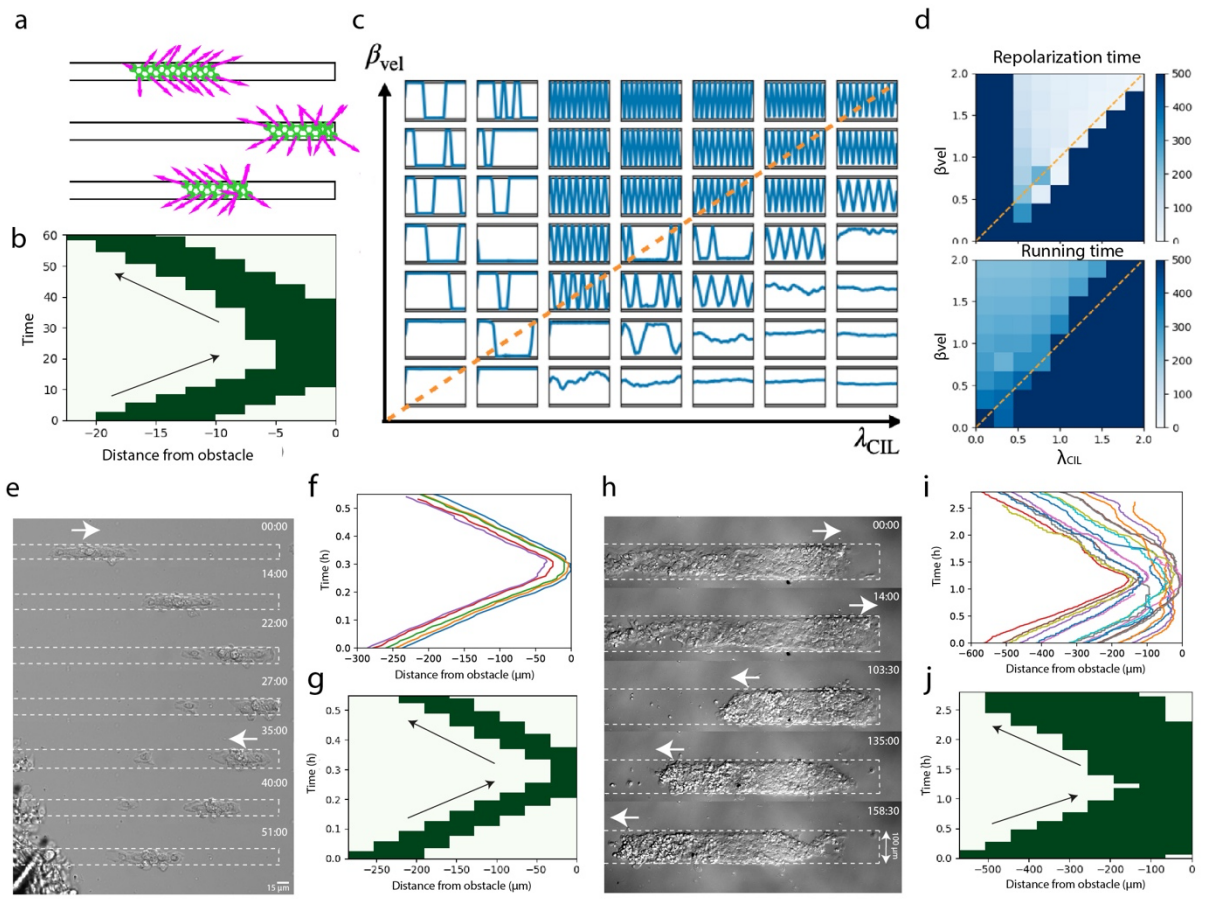

Extended Data Figure 6 – Perturbation of the polarization of epithelial cell clusters by migrating against an obstacle. (a) Theoretical simulation of the migration of a one-dimensional epithelial cluster migrating from the left to the right towards an obstacle. By using the combination of VA+PA+CIL we can observe that the cell train repolarizes towards the opposite direction after the collision. **(b)** Kymograph of the spatial position over time of the simulated cell train in (a), showing its repolarization after the collision. The slopes before and after the collision indicated similar migrating velocities. **(c)** Phase diagram showing trajectories of cell cluster center of mass in obstacles at both ends of the microstrip, as a function of the interaction parameters β_{vel} and λ_{CIL}. **(d)** Phase diagrams of repolarization and running times as a function of β_{vel} and λ_{CIL}, quantifying the repolarization and running phases in panel c. **(e)** Time-lapse sequence of the migration of a one-dimensional cluster moving towards the border of a 15 μm-wide fibronectin microstripe (from left to right) during 51 min. After reaching the micropattern extremity on the left part, the cell train compacted against the border, then

epithelial cells repolarized, and the cluster migrated in the opposite direction (from right to left). **(f)** Distance travelled over time by individual cells within the cell train presented in (e). Each color-coded line corresponds to one cell. **(g)** Kymograph of the spatial position over time of the cell train presented in (e), showing its repolarization after the collision. The slopes before and after the collision indicated similar migrating velocities. **(h)** Time-lapse sequence of the migration of a 100 µm wide epithelial cluster moving towards the border of a fibronectin microstripe (left to the right) during 158 min. After reaching the micropattern extremity on the left part, the wide cluster compacted against the border, then epithelial cells repolarized and the whole cluster migrated in the opposite direction (right to left). **(i)** Distance travelled over time by individual cells within the 100 µm wide cluster presented in (h). Each color-coded line corresponds to the one cell. **(j)** Kymograph of the spatial position over time of the 100 µm wide cluster presented in (h), showing its repolarization after the collision. The slopes before and after the collision indicated similar migrating velocities.

Supplementary Movie S1. Time-lapse sequence in DIC mode of a polarized one-dimensional cluster (7 polarized cells) that migrated on a 15 µm wide fibronectin micropattern. The scale bar is 10 µm.

Supplementary Movie S2. Time-lapse sequence in DIC mode of a polarized one-dimensional cluster (10 polarized cells) that migrated on a 15 µm wide fibronectin micropattern. The scale bar is 10 µm.

Supplementary Movie S3. Time-lapse sequence in epifluorescence mode of epithelial keratocytes labelled with the MitoTracker (MT) Red dye. Cells were detached from the front edge of primary tissue growing from the fish scale. The fluorescence intensity of the dye was proportional to the mitochondrial membrane potential. Unpolarized and stationary cells showed a low MT fluorescence intensity, which increased immediately with their polarization and migratory state. Cells were digitized in 256 bits and the MT intensity was color-coded (from high to low: white, purple, red, orange, yellow, green, light blue and dark blue). The total duration time is 1 hour and 59 minutes.

Supplementary Movie S4. Time-lapse sequence in DIC mode of a polarized epithelial cluster that migrates on a 35 µm wide fibronectin micropattern. The scale bar is 25 µm.

Supplementary Movie S5. Time-lapse sequence in DIC mode of polarized epithelial cluster that migrates on a 50 µm wide fibronectin micropattern. The scale bar is 25 µm.

Supplementary Movie S6. Animated simulations of the model with single interaction types; from top to bottom: polarity alignment (PA), velocity alignment (VA), stress-polarity coupling

(SPC), contact inhibition of locomotion (CIL). Green dots: cell positions, green lines: elastic links between cells, magenta arrows: polarities. Cells were initialized with random polarities.

Supplementary Movie S7. Animated simulations of the model with pair-wise combinations of interactions; from top to bottom: VA+SPC, PA+SPC, VA+CIL, PA+CIL. Green dots: cell positions, green lines: elastic links between cells, magenta arrows: polarities. Cells were initialized with random polarities.

Supplementary Movie S8. Animated simulations of the model combining velocity alignment, polarity alignment, and contact inhibition of locomotion (VA+PA+CIL). Green dots: cell positions, green lines: elastic links between cells, magenta arrows: polarities. Cells were initialized with random polarities. From top to bottom, systems with increasing width are shown, corresponding to n = 1,2,3,4 cells.

Supplementary Movie S9. Animated simulations of the repolarization behavior of model in a confined system with various interaction mechanisms. From top to bottom, the interaction mechanisms PA, VA, VA+CIL, VA+PA+CIL are shown. Green dots: cell positions, green lines: elastic links between cells, magenta arrows: polarities. Cells were initialized with random polarities.

Supplementary Movie S11. Animated simulations of the model combining velocity alignment, polarity alignment, and contact inhibition of locomotion (VA+PA+CIL), with parameters that capture the qualitative behavior of MDCK cell clusters. Top: microstripe (open boundary conditions). Bottom: microring (periodic boundary conditions). Green dots: cell positions,

green lines: elastic links between cells, magenta arrows: polarities. Cells were initialized with random polarities.